**Characterisation of a stratigraphically constrained gas hydrate system along the western continental margin of Svalbard from Ocean Bottom Seismometer data.**

Anne Chabert[1] (a.chabert@noc.soton.ac.uk), Tim A. Minshull[1], Graham K. Westbrook[1,2], Christian Berndt[1,3], Kate E. Thatcher[2,4], Sudipta Sarkar[1].

[1] National Oceanography Centre Southampton, University of Southampton, European Way, Southampton SO14 3ZH, UK

[2] School of Geography, Earth & Environmental Sciences, University of Birmingham, Edgbaston, Birmingham B15 2TT, UK.

[3] IFM-Geomar, Wischhofstr. 1-3, 24148 Kiel, Germany

[4] Department of Earth Sciences, Durham University, Durham DH1 3LE, UK

## Abstract

The ongoing warming of bottom water in the Arctic region is anticipated to destabilise some of the gas hydrate present in shallow seafloor sediment, potentially causing the release of methane from dissociating hydrate into the ocean and the atmosphere. Ocean-bottom seismometer (OBS) experiments were conducted along the continental margin of western Svalbard to quantify the amount of methane present as hydrate or gas beneath the seabed. P- and S-wave velocities were modelled for five sites along the continental margin, using ray-trace forward modelling. Two southern sites were located in the vicinity of a 30 km long zone where methane gas bubbles escaping from the seafloor were observed during the cruise. The three remaining sites were located along an E-W orientated line in the north of the margin. At the deepest northern site, $V_p$ anomalies indicate the presence of hydrate in the sediment immediately overlying a zone containing free gas up to 100-m thick. The acoustic impedance contrast between the two zones forms a bottom-simulating reflector (BSR) at approximately 195 m below the seabed. The two other sites within the gas hydrate stability zone (GHSZ) do not show the clear presence of a BSR or of gas hydrate. However, anomalously low $V_p$, indicating the presence of free gas, was modelled for both sites. The hydrate content was estimated from $V_p$ and $V_s$, using effective-medium theory. At the deepest northern site, modelling suggests a hydrate concentration of 7-12%, if hydrate forms as part of a connected framework, and about 22% if it is pore-filling. At the two other northern sites, located between the deepest site and the landward limit of the GHSZ, we suggest that hydrate is present in the sediment as inclusions. Hydrate may be present in small quantities at these two sites (4-5%). The variation in lithology for the three sites indicated by high-resolution seismic profiles may control the distribution, concentration and formation of hydrate and free gas.

## 1. **Introduction**

Gas hydrates are ice-like crystals that form naturally at high pressure and low temperature in continental margin sediments at water depths greater than about 300 m and in permafrost areas, whenever there is enough methane and pore water. They play a key role in the fluid flow activity and potentially in the slope stability of continental margins. Furthermore, dissociation of hydrate may trigger the sudden release of large amounts of methane through the ocean into the atmosphere, leading to accelerated climate warming. Hydrate dissociation and gas release to the atmosphere have been proposed as significant mechanisms to explain the rapid and significant climate change in the geological record [e.g., *Archer and Buffett*, 2005; *Dickens*, 1999; *Kennett et al.*, 2000; *Kvenvolden*, 1993] . This hypothesis has been challenged by other studies, that suggest that methane from dissociating hydrate may never have reached the atmosphere [*Kvenvolden*, 1999; *Sowers*, 2006]. Alternatively it has been proposed that methane release may follow, rather than lead, climate change [*Nisbet*, 2002].

Gas hydrates and free gas have been widely recognised in the Arctic [*Andreassen et al.*, 1995; *Westbrook et al.*, 2008] where the bottom-water is expected to warm rapidly over the next few decades [*Dickson*, 1999; *Johannessen et al.*, 2004]. This warming would affect the stability of shallow gas hydrate, where it exists. The region close to the intersection of the base of the gas hydrate stability zone (GHSZ) with the seabed is more likely to be affected by a bottom-water temperature warming than the deeper parts of the GHSZ [*Mienert et al.*, 2005]. Gas hydrates in this intersection zone are close to their limit of stability and will respond quickly to the anticipated Arctic warming of the Arctic region because thermal diffusion times through any overlying sediment are short. Recent models have suggested that shallow and cold deposit can be very unstable and release significant quantities of methane under the influence of as little as 1°C of seafloor temperature increase [*Reagan and Moridis*, 2008].

The recent discovery of more than 250 gas bubble plumes escaping from the seabed along the West Spitsbergen continental margin, in a depth range of 150-400 m, provides direct evidence for ongoing methane release [*Westbrook et al.*, 2009] (Figure 1). It probable that many of the plumes are directly fed by the primary geological methane source in this area [*Westbrook et al.*, 2009]. Although acoustic images of the bubble plumes show very few that reach the sea surface, and even for these it is probable that nitrogen and other gases would have largely replaced methane in the bubbles during their ascent [*McGinnis et al.*, 2006], nevertheless some methane will transfer to the atmosphere by equilibration of methane in solution in sea water.

The presence of hydrate and free gas is commonly interpreted from the observation of a bottom-simulating reflection (BSR). The BSR is a composite hydrate/gas reflection, and its amplitude is principally sensitive to the presence of free gas at the hydrate phase boundary [*Holbrook et al.*, 1996;

*Singh et al.*, 1993]. Therefore, the BSR indicates the likely presence of hydrate above the BSR, but yields little direct information about its concentration or distribution. However, detailed information on the concentration and distribution of hydrate can be inferred from the seismic properties of the sediments. Pure methane hydrate has a P-wave velocity (Vp) of ~3.8 km/s and S-wave velocity (Vs) of ~1.96 km/s [*Helgerud et al.*, 2009]. Consequently, the presence of hydrates can increase the P- and S-wave velocities of the sediment. Conversely, the presence of free gas in the pore space will significantly decrease the P-wave velocity, while the S-wave velocity will change little.

To develop a better understanding of the distribution, concentration and formation of hydrates, a range of seismic techniques has been tested recently off the coasts of Svalbard and Norway. The results from the HYDRATECH project [*Westbrook et al.*, 2008] have shown that using seabed arrays of four-component ocean-bottom seismometer (OBS) units with dense shot patterns, Vp and Vs in a region of hydrate occurrence can be determined with sufficient accuracy to discriminate confidently variations of hydrate saturation greater than 3–7% of pore space, depending on the model for the effect of hydrate on seismic velocity.

Once velocity as a function of depth has been defined, methods for determining hydrate saturation normally require the definition of a background velocity function, which would be expected in the absence of hydrate. Where the measured velocity is higher than the background velocity, hydrate is inferred to be present and its saturation is estimated from rock physics models of how the presence of hydrate in the sediment affects the seismic velocity.

The objective of this paper is to determine the distribution of hydrate and free gas at five representative sites along the continental margin of Western Svalbard. Our OBS experiments were designed to investigate the upper limit of the GHSZ as well as deeper sites where the BSR was observed in the seismic reflection profiles. This work will enable us to quantify how much methane has accumulated in the critical area at the base of the GHSZ along the continental margin of Western Svalbard, and therfore constrain the potential future gas release from the zone of hydrate instability.

## 2. **Western Svalbard – Geological setting**

The continental margin west of Svalbard formed by progressive south to north oblique rifting between Eurasia and Laurentia throughout the Tertiary [*Faleide et al.*, 1993]. The tectonic setting of the study area is characterized by the transition from a young passive margin in the south to a transform margin segment along the Molløy transform fault and fracture zone west of the Kongsfjorden cross-shelf trough then to another rifted margin segment east of the Molløy Deep underlying the contouritic Vestnesa Ridge (Figure 1). South of the Molløy Fracture Zone the active Knipovich Ridge formed in Early Oligocene times as a response to a change from an early strike slip to a later rift setting with oblique spreading ultimately leading to the continental break-up of Svalbard from Greenland [*Harland et al.*, 1997].

The Late Cenozoic post-rift evolution of sedimentary basins in the Arctic region is closely linked to the action of glaciers, which respond rapidly to fluctuations in climate. Sediments on the west Svalbard margin are either glacigenic debris flows in trough-mouth fans beyond the shelf break [Vorren and Laberg, 1997; Vorren et al., 1998] or turbiditic, glaciomarine and hemipelagic sediments, partly reworked by contour currents [*Eiken and Hinz*, 1993; *Sarkar et al.*, 2011; *Vorren et al.*, 1998].

On the Yermak Plateau and along the Vestnesa Ridge, three sedimentary sequences have been observed [*Myhre et al.*, 1995]. The bottom YP1 sequence consists of syn- and post-rift deposits above oceanic crust, whereas contourites characterize the overlying YP2. The YP2/YP3 unconformity, defines the onset of the Plio-Pleistocene glaciations and deposition of glacially derived material on the upper slope in the Kongsfjorden Trough Mouth Fan (TMF) [*Vorren and Laberg*, 1997].

There is ample evidence for active fluid migration systems along the continental margin west of Svalbard. Widespread pockmark fields and pipe structures occur on the Vestnesa Ridge [*Vogt et al.*, 1994]. Furthermore there is a strong and widespread BSR [*Eiken and Hinz*, 1993]. Further evidence for the presence of hydrate was later coprovided by ocean bottom hydrophone work [*Mienert et al.*, 1998] and the HYDRATECH OBS survey [*Westbrook et al.*, 2008]. Based on results from these previous studies on the Vestnesa Ridge and southwards, hydrates are likely to be found above the R3 regional unconformity, which belongs to the YP3 sequence deposited since 0.78 Ma [*Eiken and Hinz*, 1993]. The velocities from the HYDRATECH OBS experiment suggest that the sedimentary pore space in this area contains up to ~10% hydrate.

## 3. **Seismic acquisition**

In August-September 2008, we carried out a seismic experiment along the western continental margin of Svalbard using OBS and high-resolution seismic reflection methods. The OBS acquisition was designed to record P- and S-wave reflections in the first few hundred meters of the sedimentary sequence where the base of the GHSZ is expected in this region. The seismic source comprised two 150 $in^3$ GI air guns (45 $in^3$ generator and 105 $in^3$ injector). OBSs from the UK Ocean Bottom Instrumentation Facility [*Minshull et al.,* 2005] were fitted with three-component geophones and one hydrophone recording with a sampling frequency of 1 kHz. Several instruments were deployed at each of five sites on the margin to allow for possible instrument failure and to account for lateral variations. The OBSs were placed at ~200 m intervals and shots were fired out to a range of a few kilometres either side on lines in several directions, with a regular shot spacing of 5s (~12.5 m). The BSR distribution was determined from multi-channel seismic profiles acquired during the survey. The multi-channel seismic data were recorded with a 600 m-long 96-channel streamer owned by the University of Århus.

The data were processed including post-stack time migration with a 3.125 m CDP spacing [Sarkar et al., 2011]. Two sites were chosen in the southern area, and three OBSs and four OBSs were deployed at sites $S_1$ and $S_2$, respectively. These southern sites lie in a water depth of 480-350 m at the bottom of the continental slope. Site $S_2$ is located below the upper limit of the gas hydrate stability zone (GHSZ) whereas site $S_1$ is located landward of the upper limit of the GHSZ, in the plume field area (Figure 1). High-resolution seismic reflection profiles acquired along the southern sites show that the GHSZ lies within glaciomarine sediments in this area.

The northern acquisition was designed along a straight line going from 1280 m depth in the oceanic basin to about 300 m depth on the continental shelf. Two OBSs were deployed at each of the three different sites ($N_1$, $N_2$, and $N_3$) along this line. Site $N_3$, the deepest, is underlain by contourite sediment based on the seismic reflection profile shot at the site. This site was chosen because a clear BSR is observed there. Site $N_2$ is at about 860 m depth and lies above a stacked glacio-marine package. The shallowest northern site, $N_1$, is on the continental shelf and above the upper limit of the GHSZ.

## 4. P- and S- wave velocity modelling

To infer the occurrence of gas hydrate and free gas within the sediments, vertical and lateral variations in seismic velocity were analysed based on reflection traveltimes. P-wave reflections were observed on all 13 OBSs deployed. An example of reflections from OBS 5 (site $N_3$) is shown in Figure 2. Hydrophones generally gave the largest signal-to-noise ratio and were used for picking of reflected phases. Up to eight reflections were picked from the deepest site in the basin ($N_{3)}$, including the BSR (Figure 2), while five and six reflections were picked on the two sites with the higher signal-to-noise ratio, both located on the shelf break ($S_1$ and $N_1$). Before modelling each pick was assigned an uncertainty, corresponding to possible picking error due to the quality of the data. The picking error usually corresponds to the width of the reflection peak. For the P-wave dataset the uncertainties vary between 2 and 10 ms.

The multi-component data also enabled the identification of P-S converted waves. Previous examples of the identification of P-to-S converted waves offshore Svalbard were given in *Haacke and Westbrook* [2006] and *Haacke et al.* [2009] Observations of the P-S converted waves were made on the radial component, which is a vector combination of the two horizontal geophone records in the direction of the shot. S-wave reflections were more difficult to pick due to the presence of low frequency noise. Indeed, the combination of a large and heavy OBS packages with very soft water-saturated sediments that they were deployed in produce low frequency resonance noise, which can mask the P-S converted waves. S-waves have a lower dominant frequency than the P-waves, especially in unconsolidated sediments at the seafloor, where they are also strongly attenuated. S-wave reflections were picked only for OBS at sites S2, N2 and N3. Their assigned uncertainties vary between 4 and 12 ms.

The reflected waves were then modelled using a forward modelling technique [*Zelt and Smith*, 1992] by fitting the calculated reflections in a user-defined model to the observed reflections on the OBS sections. P-wave reflections were modelled using a layer-stripping approach from the top to the bottom and the different interfaces were adjusted until a good fit was found with the calculated data. The S-wave reflections were then modelled using the well-constrained P-wave velocity model. The P-wave velocity model was fixed such that the only parameter perturbed was the Poisson Ratio [*Zelt and Smith*, 1992]. The S-wave reflections were matched to the modelled P-wave reflections by an error/trial method until the best fit (i.e lower traveltime residuals) between the observed and calculated data was found. For each site, two lines, perpendicular to each other, were modelled (Figure 1). Examples of P- and S-waves velocity models at site $N_3$ are given in Figure 3.

The spatial resolution of the velocity models is limited by the number of OBS deployed (two to four at each site) and the spacing between the instruments (~200 m intervals). Consequently there were significant limits on the ray coverage and spatial resolution of the models away from the central portion of the models (Figure 3). Vertical and horizontal nodes in the model are sparsely spaced at ~20-100 m and ~200-500 m, respectively. The horizontal node spacing is similar to the spacing of the OBSs, which provides an approximate estimate of lateral resolution [*Zelt*, 1999].

The final model was considered to be satisfactory when its root-mean-squared (RMS) travel-time residual was within the range of the uncertainties of the picks. Our approach for the $\chi^2$ statistic was to maintain a well-resolved but relatively coarsely parameterised model and accept a final $\chi^2$ value greater than 1 to avoid over-parameterisation. Statistics for each model are shown in Table 1.

The F-test statistical analysis [*Press et al.*, 1992] was applied to the model parameters at site $N_3$ to provide an estimate of the velocity uncertainty in the final velocity model. Velocities were adjusted for each layer while maintaining the velocity gradient. Perturbed models are considered different from the final model when the variation in $\chi^2$ is significant at the 95 per cent confidence limit. The P-wave velocity uncertainty in the eight layers of the model for site $N_3$ varies from ±0.01 km/s for the shallowest layer to ±0.06 km/s for the deepest layer (Figure 3).

## 5. **Seismic Results**

### 5.1 **P- and S-wave velocities**

At site $N_3$, a clear decrease of the P-wave velocity is observed about 195 m below the seafloor, where the velocity decreases from 1.84 to 1.5 km/s (Figure 4). This low velocity zone is 55 m thick and indicates the presence of free gas in the sediment. This zone lies below a zone of higher than normal P-wave velocity. The top of this high velocity zone is observed about 130 m below the seafloor, with an average velocity of 1.82 km/s in the layer. The impedance contrast between the two layers forms a bottom simulating reflection (BSR), which is observed on the seismic reflection profile at this site (Figure 3). P-wave velocity models for this site are very similar to those from the HYDRATECH experiment [*Westbrook et al.*, 2008], which was carried out on the west Svalbard margin at a similar water depth (Figure 1). An S-wave high-velocity zone from 130 to 195 m below seafloor (bsf) is also seen at site $N_3$, coincident with the zone of higher P-wave velocities. The S-wave velocity in this zone is about 0.46 km/s and this velocity decreases below the BSR to 0.41 km/s. These high velocities above the BSR are attributed to hydrate in concentrations high enough, and sufficiently coupled to the sediment frame, to affect the shear strength of the sediments. Previous studies have shown that $V_s$ can be increased by the presence of hydrate, when hydrate cements the grains and/or supports the grain framework [*Chand et al.*, 2004]. S-wave velocity changes little when pore water is replaced by free gas. Comparison between the P-wave velocity model and the seismic reflection profile (Figure 3) suggests that the distribution of gas hydrate and free gas in the sediment is relatively uniform above and below the BSR. A P-wave low velocity anomaly, as seen at site $N_3$, is also observed at sites $N_2$ and $S_2$ (Figure 4). These decreases in the P-wave velocities (of 0.15 km/s at 365 mbsf and 0.25 km/s at 160 mbsf, for sites $N_2$ and $S_2$, respectively) suggest the presence of free gas.

Based on the depth of the base of the GHSZ observed in the seismic data and the sea-bottom temperature of –0.8°C from nearby CTD measurements, it is possible to estimate the geothermal gradient at site $N_3$. Pressure at the base of the GHSZ was calculated assuming a hydrostatic pressure gradient within the sediments. The pressure/temperature stability curve for methane hydrate in seawater (water of 3.5% salinity) [*Moridis*, 2003] was then used to calculate the temperature at the base of the GHSZ and, hence, derive a geothermal gradient of 83.5°C/km, assuming that this gradient is linear from the sea bed to the base of the GHSZ. At site $S_2$, the hypothesis of a base of GHSZ at 160 mbsf would suggest a thermal gradient of 33°C/km (for a sea bottom temperature of 2.5°C), which is very low for a site located 50 km east of the Knipovich ridge. Therefore we conclude that the velocity anomaly is too deep to represent the base of the GHSZ and it is interpreted as a gas pocket beneath a low permeability layer. The seismic reflection profile at this site shows discontinuous and, in places, chaotic reflectors of generally high amplitude, characteristic of the glaciogenic sediment sequence, above the low velocity zone, which is lies within and is underlain by more continuous, lower amplitude reflectors, typical of hemipelagic sediments and which exhibits greater attenuation of higher frequencies in this area than it does farther down slope, indicative of the presence of gas (Figure 5). At site $N_2$, seismic reflection sections locally show with a lower frequency response at and below the depth where a gas pocket is interpreted, which is consistent with the presence of gas-charged sediments (Figure 5). These seismic results suggest that gas is present in the form of pockets in the sediment at variable depths. However, there was no unambiguously high seismic velocity at sites $N_2$ and $S_2$ that could be interpreted to indicate the presence of hydrate.

### 5.2 **Vp/Vs analysis**

The relationship between P- and S-wave velocities, as well as the Poisson Ratio, provide further constraints on the presence of hydrate and free gas in the sediment. A crossplot of $V_s$ versus $V_p$ discriminates hydrate-bearing and gas-bearing sediments (Figure 6). Site $N_3$ shows a low $V_p$ and high

$V_s$ where free gas is present in the sediment below the BSR, even to depths approaching 200 m below the BSR.

At site $N_2$, the $V_p/V_s$ crossplot highlights a 70-m-thick sedimentary layer with low $V_s$ at about 180 m below the sea floor (Figure 6). As S-waves mainly respond to the sediment matrix, we suggest that this low $V_s$ is the result of a loosening of the grain contacts and hence a reduction of rigidity. This rigidity reduction indicates that sediments at this depth form a low permeability unit in which fluid pressure has remained high during sedimentation at a high rate, because the water could not drain from it easily. At this site, based on thermal modelling, with an identical thermal gradient and sea-bottom temperature slightly higher to the ones deduced from site $N_3$, located 10 km away, the base of GHSZ is predicted to be around 180 m below the seafloor. This depth matches the depth of the upper limit of the low-$V_s$ layer., which is, therefore, attributed to under-compactions. However, questions remain on why the loosening of the grains does not decrease significantly Vp.

The $V_p/V_s$ analysis may be used also to define reference velocities for the hydrate-free sediments. This is achieved by using a specific empirical relationship for our study based on the modelled P- and S-wave velocities. A least-squares fit between velocity and depth can be calculated, ignoring the values from the hydrate- or gas-bearing sediments. Such an empirical relation could not be defined for site $N_2$, as only one $V_p/V_s$ value was left after discounting the gas-bearing deepest layer. The results for sites $N_3$ and $S_2$ are shown on figure 6. The reference velocity for contourites (i.e. site $N_3$) is, as expected, lower than for the mixture of hemipelagic and glacigenic debris flow sediments at the same depth (Figure 6). These relationships are valid only for the regional depositional environment.

## 6. **Disseminated gas hydrate and free gas concentration estimation**

A key step in the process of remotely determining hydrate content is determining a quantitative relationship between that content and the physical properties measured (i.e., the seismic velocities). The respective amounts of hydrate and free gas can be quantified by comparing the observed deviations of these properties from those predicted for sediments where no gas hydrate or free gas is present, since the presence of gas hydrate increases $V_p$ and $V_s$ and the presence of free gas decreases $V_p$. Several rock physics-based approaches exist to estimate to concentration of gas hydrate in the sediment including the self consistent approximation/differential effective medium (SCA/DEM) approach [*Chand et al.*, 2006; *Jakobsen et al.*, 2000] and the three-phase effective medium model (TPEM) [*Ecker et al.*, 1998; *Helgerud et al.*, 1999]. Each of these approaches involves different simplifying assumptions regarding the shapes of individual sediment components and the way in which they interact with each other. All assume that, on the scale of a seismic wavelength, there is a degree of uniformity in the hydrate distribution, and that hydrate is disseminated in some way through the pore space. Hence none of these approaches copes well if hydrate occurs dominantly in nodules or veins [*Minshull and Chand*, 2009]. For disseminated hydrate, the modelling can be carried out as follows [*Ecker et al.*, 1998]: (1) Gas hydrates fill the pore space and are modelled as part of the pore fluid. In this case the solid gas hydrate has no effect on the stiffness of the dry frame (pore fluid model) [*Helgerud et al.*, 1999]; (2) hydrate act as inter-granular cement and forms a connected load-bearing frame (frame-only model); (3) part of the hydrate forms a load-bearing frame and the remainder form pore-filling inclusions (frame-plus-pore model) [*Chand et al.*, 2006]. The model assumes that the sediment grain connectivity is a function of porosity. In the model used, the proportion of hydrate forming an inter-granular cement increases linearly with the hydrate saturation, so that, for example, at 1% of hydrate saturation, 1% of the hydrate is part of the load-bearing frame. Therefore, if the hydrate saturation is low, the pore-plus-frame model has a low proportion of cementing hydrate and it becomes difficult to distinguish between the pore-plus-frame model and the pore fluid model.

Using the three-phase effective medium (TPEM) approach of *Helgerud et al.* [1999], we calculated the hydrate saturation assuming that hydrate forms part of the pore fluid. In this case, the assumption is that hydrate and water are homogeneously distributed throughout the pore space; therefore, the increase of velocity with hydrate saturation is gradual and the elastic properties remain close to those of unconsolidated sediments. The TPEM approach can be used also when hydrate is a load-bearing component of the frame; however, this load-bearing framework model does not take into account any component variability in the load-bearing effect. Therefore, another approach was chosen to define the hydrate saturation for the load-bearing frame model. The SCA/DEM approach of *Chand et al.* [2006] was chosen for the frame and frame-plus-pore models. This approach uses the self-consistent approximation (SCA) to create a bi-connected composite. A differential effective medium (DEM) theory is then applied to fine-tune the sediment component proportions. For the frame and pore-plus-frame models, the SCA medium starts with hydrate as part of the matrix. Hydrate can then be added as a part of the load-bearing framework, so that the grains of sediment are replaced by grains of hydrate, or/and hydrate forms inclusions. For the frame model, only a small amount of hydrate increases the elastic velocity significantly, and the elastic properties of hydrate-bearing sediments approach those of consolidated sediments.

Using the *Helgerud et al.* [1999] approach, we also estimated the concentration of free gas below the BSR. These authors proposed two different models. The first assumes a homogenous gas distribution in suspension in the pore fluid; the second assumes a patchy distribution of fully gas and fully water-saturated sediment. In the suspension model each pore has the same proportions of gas and water. Formally the same TPEM method as for the hydrate concentration is applied. In the case of patchy distribution, the pore space is supposed to consist of neighbouring regions of fully gas saturated and fully water saturated regions on a length scale much larger than the pore size, but much smaller than the seismic wavelength. Both approaches were applied on the data to model free gas.

### 6.1 **Site $N_3$**

As explained above, the hydrate saturation is inferred from the seismic observations and is dependent upon the function representing the background variation of $V_p$ and Vs with depth, in the absence of hydrate. It is, therefore, important to choose background velocities that are coherent with the observed data as they cannot be constrained by any borehole data. Two different background velocities were used for site N3 to test the sensitivity of the choice of the background velocities upon the estimation of gas hydrate concentration. The average P- and S-wave velocity/depth curves for terrigenous sediments of Hamilton [1980] were first used as background-velocity functions for the purpose of comparison. There is no *a priori* reason to expect that these functions are appropriate, beyond that they are broadly representative of the behaviour of the fine-grained terrigenous sediment that occur at the site. The second background velocity tested is a smoothed average of the velocity depth curves for OBSs 5 and 6 based on the interpretation that the velocity increase above the BSR is due to the presence of hydrate and the velocity decrease below the BSR is due to the presence of free gas (Figure 7). To ensure that the model predicts the background velocities when no hydrate is present, we adjusted the model clay contents such that the correct background velocities were predicted when the porosities corresponded to densities that are related to the velocities by Hamilton's terrigenous relation [*Hamilton*, 1980]. The obtained porosity at each site is plotted against the porosity from the nearby ODP986 in order to check the reliability of our values (Figure 7). The background velocity and porosity values are also given in Table 2. The results suggest that hydrates are present in large quantities in the sediment above the BSR. Hydrate saturation in the pore space is up to 22% for the pore fluid model, up to 12.6% for the frame-plus-pore model, and up to 7% for the frame model. However, because the S-wave velocities increase strongly above the BSR, we infer that hydrates are at least partially load-bearing and therefore, the result for the pore fluid model is dismissed. The highest concentration of hydrate is in a 50 m thick layer above the BSR in which the saturation of hydrate varies between 7% and 12.6%. The inferred saturation is slightly greater when using the Hamilton curves as background velocities. In the layer above the BSR, $V_s$ is identical for the two background velocities, and $V_p$ is 0.2 km/s higher for the average velocity based on the OBS data than for the Hamilton curve, the discrepancy between the results for the hydrate saturation is less than 1.5%. The results for site $N_3$ are comparable with the estimates of hydrate saturation at the HYDRATECH site [*Westbrook et al.*, 2008] which predicted between 6 and 13 % of hydrate in the sediment using an identical approach.

Free gas concentration was also estimated below the BSR using the *Helgerud et al.* [1999] approach and the two different background velocities. The results for the uniform mixture and the patchy distribution models differ significantly. The uniform mixture model predicts a very small amount of free gas (~1%) in the 50 m thick layer below the BSR. This reflects that a minimum amount of free gas is necessary to decrease the P-wave velocity dramatically. In contrast, the patchy distribution model estimates a gas saturation of 6.5% in this layer.

### 6.2 Sites $N_2$ and $S_2$

At site $N_2$, Vp and Vs modelling did not suggest any strong increase of the velocities that might be attributed to hydrate. This result suggests that either there is no hydrate at this location, reinforcing the idea of a patchy distribution, or that the amount of hydrate is too small to be resolved. As we have seen before at site $N_3$, a small quantity of hydrate is sufficient to increase significantly the P-wave velocity when the hydrate forms part of the load-bearing framework. In contrast, for the pore fluid model, a large quantity of hydrate in the sediment is required to increase the velocity significantly. Based on this observation, we infer that if significant hydrate is present in the sediment at site $N_2$, it must be present in the pore fluid and not as part of the load-bearing frame. The three approaches were, however, used to demonstrate that, in any case, they cannot be a very large amount of hydrate present in the sediment at these sites. To define background velocities, Hamilton curves were not used as their values were too low compared to the modelled velocities (Figure 7). A similar strategy as for site $N_3$ was implemented (values are given in Table 2). When hydrate is present in the pore fluid it does not affect the shear modulus, so the S-wave background velocity is identical to the observed S-wave velocity. However, S-wave reflections were only modelled to about ~250 m below the seafloor. Beyond this depth the Vp/Vs relationship for hydrate- and gas-free sediment deduced for site $N_2$ was used (Figure 6). For the pore fluid model the hydrate saturation is inferred to be around 4% in a 115 m thick layer above the base of the GHSZ, which is about 180 m below the seabed. Below the GHSZ, the gas saturation is around 2% for patchy distribution and around 0.2% for the uniform distribution. Seismic modelling suggests a low velocity zone about 365 m bsf at this site. If this zone is due to the presence of gas, the saturation is around 2.5% for patchy distribution and around 4.5% for the uniform distribution. This result suggests that the concentration of free gas is higher in this deeper layer than just below the base of the GHSZ.

Similarly no strong increase in the velocity was observed for the southern site $S_2$. There is a strong decrease in velocity at a depth of about 160 m but this is too deep to represent the base of the GHSZ. Using the same approach as that for the site $N_2$, we estimate the concentration of disseminated hydrate above the base of the GHSZ at about 4.8%. Free gas is also present in the sediment below the base of the GHSZ (3.5% and 0.1% for the patchy and the uniform distribution models, respectively). A low velocity zone interpreted as a gas pocket is suggested at about 160 m bsf from the P-wave velocity model at this site. We modelled the gas saturation for this layer between 3.2 and 8.5%, which is nearly 3 times the estimate of gas saturation for the layer just below the GHSZ. This layer is interpreted as gas pocket forming underneath less permeable sediments.

Because of the lack of appropriate control from nearby boreholes, the $V_p$ and $V_s$ background functions, and hence the velocity anomalies caused by hydrate are difficult to define. The uncertainty in the background velocity and porosity is a major cause of uncertainty in estimating the amount of hydrate present, such that the presence of hydrate could easily be overlooked or erroneously predicted. An increase of 10 m/s of the P-wave background velocity decreases the hydrate content by 1% for the pore fluid model and the pore-plus-frame model and 0.5% for the frame model.  An increase of 10% in the asumed the porosity decreases the hydrate content by 3% for the pore fluid model and pore-plus-frame model and 2% for the frame model In these cases, the presence of a BSR is the most reliable indicator of the presence of hydrate, although it provides little to no information on the amount of hydrate that is present.

## 7. **Gas hydrate concentration estimation in nodules or veins**

From several cores of fine-grained clay-rich mud sampled at *in situ* pressure from offshore India and South Korea [*Schultheiss et al.*, 2009] it has been observed that hydrate occupies networks of veins with a few centimetres separation. To estimate the concentration of hydrate in the sediment on the Svalbard margin, if hydrate occupies bedding planes and fractures, we used a simple time-average approach [*Plaza-Faverola et al.*, 2010]. The approach consists of comparing the obtained seismic velocities to their background velocities for each layer to derive estimates of the proportion of sediment locally occupied by hydrate-filling veins. This approach does not take into account mineral content or S-wave velocities and is based on two different end-member assumptions. The first assumption is that hydrate is an addition to the host sediment. This means that gas and water forming the hydrate are introduced to the GHSZ, displacing the sediment without changing the water content, porosity, or mechanical properties of the host sediment. The second assumption is that only free gas is introduced to the GHSZ so the water needed to form hydrate must come from the host sediment, thus reducing the water sediment content and porosity of the host.

Results for the three sites are given in Figure 8. The background velocity function used is identical to the ones used for the disseminated models. At site $N_3$ the modelling yields an estimate of hydrate saturation above the BSR of 10.3% with the additional-water model, and around 5% with the water-from-host model. At site $N_2$, the additional-water model and the water-from-host model predict 0.6-0.8% and 1.6-1.8% of hydrate saturation as a fraction of the total volume, respectively. For the southern site, hydrate saturation in the sediment varies between 0.3-1.9% for the water-from-host model and 0.6-2.1% for the additional-water model.

For the second assumption, in which water is removed from the surrounding sediment, the percentage of hydrate is lower due to the fact that less hydrate is needed under the second assumption to produce velocity anomalies. These models predict less hydrate for a given velocity anomaly than the disseminated pore-fluid model.

## 8. **Discussion**

The large velocity variations shown at the deepest site suggest the presence of an appreciable amount of gas hydrate and free gas in the pore space of the sediments. The high resolution seismic profile at this site shows a litho-facies interpreted as contourite sediment and shows continuous stratigraphic layers and a clear BSR which can be followed over nearly 5 km (Figure 3). Similarly, P-wave velocity modelling shows no strong lateral change in the distribution of gas hydrate above the BSR. A model where hydrate acts as a load-bearing component of the sediment frame is favoured at site $N_3$ due to the increase of the shear-wave velocity above the BSR. Effective medium modelling suggests that hydrate is present from the BSR up to 60 m below the seabed, with a hydrate saturation decreasing gradually towards the seabed. Hydrate saturation averages about 7-12% above the BSR. This result is in the range of hydrate saturations previously modelled along the Svalbard margin in similar clay-rich sediment: 6-12% at the Hydratech site [*Westbrook et al.*, 2008] and up to 11% at the Vestnesa Ridge [*Hustoft et al.*, 2009]. Compared to other areas, where hydrate concentration estimates where made using a similar DEM/SCA approach with a clay-water composite as starting model and some degree of cementation, the hydrate saturation at site $N_3$ is slightly higher than those observed at southern Hydrate Ridge (ODP Leg 204, off the coast of Oregon) and Blake Ridge (ODP Leg 164, off the US east coast) which yield similar average saturations, in the vicinity of the BSR, of 3-8% and 2-7%, respectively [*Dickens*, 1999; *Holbrook et al.*, 1996; *Tréhu et al.*, 2004]. These estimates were derived using robust background velocities based on borehole data in both areas. On the basis of the analysis of *Chand et al.* [2004], an error of 10% in the assumed clay content would result in an error of ~5% in hydrate saturation. If the clay content used to define the background velocity at site $N_3$ were overestimated by 10%, then the hydrate saturation for this site would be similar to that at Hydrate Ridge and Blake Ridge.

A further complication for the models of the effect of hydrate on seismic properties, which commonly assume interactions between hydrate and its host sediment, is that in low-permeability and clay-rich sediment, as seen at site $N_3$, hydrate can occupy fractures and bedding planes [*Liu and Flemings*, 2007; *Schultheiss et al.*, 2009]. Using a simple time-average approach [*Plaza-Faverola et al.*, 2010] we modelled the estimates of hydrate concentration in nodules and veins. Results are in the range of the frame and frame-plus-pore models.

No strong evidence for hydrate-bearing sediment could be inferred from the Vp and Vs modelling at the other two sites below the upper limit of the GHSZ, $N_2$ and $S_2$, which lie on similar glacial sediments with interbedded layers of hemipelagic sediments. However, the supply of methane along the western Svalbard continental margin is inferred by the observation of gas escape from the seafloor close to the 396-m isobath [*Westbrook et al.*, 2009]. If hydrate is present in the glacio-marine sediment at these sites, it is at a concentration too low to have a strong effect on the velocities, at the resolution of our method, and does not support the sediment frame.

Small positive velocity anomalies at these sites, relative to a smooth background velocity-depth function, could be attributed to the presence of a few percent of hydrate disseminated within the pore space and/or in veins. The absence of BSRs and strong hydrate-related velocity anomalies in these glacigenic sediments is consistent with a model in which such sediments inhibit upward fluid migration and limit gas hydrate formation, as has been suggested in the southern Vøring Plateau [*Bünz and Mienert*, 2004].

From our analysis we infer that the hydrate formation and distribution vary along the margin (Figure 9). We suggest that these variations are controlled by the lithology and stratigraphy of the sediments. In particular, the porosity and permeability control fluid migration into the GHSZ, thereby controlling hydrate accumulation. These properties also appear to control the way the sediment host and hydrate interact with each other (Figure 9).

Lithological variations also affect the free gas accumulation. In the sediment below the BSR, free gas saturations are generally higher close the base of the GHSZ. At site $N_3$, the P-wave velocity model shows an uniform layer of gas below the BSR and gas content is estimated around 1-7% in the sediment. In the glacio-marine sediments (sites $N_2$ and $S_2$), the gas content in the sediment below the base of the GHSZ is much lower (0.2-2% and 0.1-3.5% for sites $N_2$ and $S_2$, respectively) confirming that gas-hydrate saturation is related to the availability of free gas. At both sites, however, we infer the presence of gas pockets beneath the base of the GHSZ. In the seismic reflection profiles, these gas pockets form continuous reflections within hemipelagic sediments. Although there is no clear relationship between these gas pockets and the concentration of hydrate, we suggest that the presence of gas pockets in hemipelagic sediments below the glacio-marine material indicates that the gas supply is sufficient for hydrate formation within the GHSZ.

When sites with similar lithology are compared (i.e. sites $N_2$ and $S_2$, and site $S_1$ and $N_1$), velocity models for the four sites along the western continental margin of Svalbard show a trend with P-wave velocities lower at the southern sites. This trend could be due to variations in lithology and/or compaction along the margin. However, we suggest that this variation could also be an indicator of presence of higher saturation of diffuse gas in the sediment in the south. The observation that Vp is lower at site $S_2$ than at site $N_2$, but Vs is similar at both sites, supports this suggestion. The presence of diffuse gas over the 500 m sedimentary sequence that is modelled would lead to a lower average Vp, but identical Vs.

## 9. **Conclusions**

From our analysis of P- and S-wave velocities, we conclude that:

1. Significant P and S-wave velocity variations occur above and below the BSR at the deepest site. These variations are related to the presence of gas hydrate and free gas, within contourite sediments. At the shallowest sites in the GHSZ, no BSR was clearly identified and limited amounts of hydrate and gas are modelled.

2. The distribution and saturation of hydrates show significant variations along the Svalbard margin. The hydrate saturation generally increases down slope as the seismic facies vary from glacio-marine

sediments to hemipelagic sediments. The average gas hydrate saturation of pore space is less than 5% at the shallowest sites and at least 7-12% at the deepest site.

3. The free gas saturation varies from 1-7% at the deepest site to less than 3.5% at the shallowest sites. Free gas accumulates just below the BSR and in gas pockets beneath less permeable layers of glacio-marine sediments. The physical and geological properties of stratigraphic layers govern the saturation of free gas.

4. The formation of gas hydrate is lithologically controlled. A model in which hydrate forms part of the sediment frame in hemipelagic sediments, probably in combination with pore filling, give the most satisfactory explanation of the seismic results. Our results do not indicate unambiguously the presence of hydrate in the glacio-marine sediments, primarily because the normal seismic velocity in these sediments is not sufficiently well known to recognise an anomalous velocity caused by the presence of hydrate. If hydrate occurred in these sediments as a few percent of the pore fill it would go unnoticed, as would hydrate filling veins that occupied a few percent of the total sediment volume. If hydrate were present in the glacigenic sediment at the same concentrations as those indicated for the hemipelagic sediments, a mode of emplacement that had a strong effect on the sediment frame should produce a noticeable velocity anomaly. Our results also suggest that in order to allow gas hydrate to form in the less permeable glaciomarine sediments, a deeper source of gas has to exist underneath the base of the GHSZ.

5. The presence of hydrate along the Svalbard continental margin indicated by seismic velocity anomalies and by the presence of a BSR at locations more than 100 km apart suggest that it is widespread on the margin. Its proximity to the landward limit of the GHSZ could have broad significance for methane release in the Arctic in response to warming of the seabed over the next few decades.

**Figure captions:**

Figure 1: Shaded-relief bathymetry and location of the seismic experiments along the Western Svalbard continental margin. Close-ups a) and b) show the OBS deployed at the five sites. The 396-m isobath is the approximate landward limit of the GHSZ [*Westbrook et al.*, 2009]. The back lines show the profiles that were modelled using P-waves for each sites, and S-waves for sites $N_3$, $N_2$ and $S_2$.

Figure 2: Hydrophone and radial components for OBS 5. Both sections have been flattened on the direct arrival for display purposes. a) P-wave reflections used for velocity modelling as seen on the hydrophone section. The BSR is indicated by a strong amplitude reflector and a change in the polarity. A bandpass filter of 5-10-200-250 Hz) was applied on the hydrophone sections to reduce the signal-to-noise ratio. b) The P-S converted waves are observed on the radial component. A bandpass filter was applied of 10-15-70-90 on the radial sections.

Figure 3: A) 2-D P-wave velocity model for site $N_3$; B) 2-D S-wave velocity model for site $N_3$. The BSR is modelled over ~3.5 km for both final models. The grey shades show the part of the models that are not constrained by the rays. C) Uncertainty in the eight P-wave velocity layers for site $N_3$. The perturbed layer is considered different from the final layer when the variation in $\chi^2$ value is significant at the 95 per cent confidence limit of the statistical F-test, represented by the vertical bars on each $\chi^2$ curve; D) 1D velocity log extracted from the above P-wave velocity model at the OBS 5/6 position is superimposed on the equivalent seismic reflection profile.

Figure 4: Compilation of the P and S-wave velocities for the five sites. Each log is extracted at the OBS locations.

Figure 5: Velocity-depth variation from sites $N_2$ and $S_2$ P-wave models, superimposed on a coincident seismic reflection profiles. The seismic profiles are shown by the back lines on Figure 1a) and b).

Figure 6: Crossplot of P- and S-wave velocities of $N_3$, $N_2$ and $S_2$ compared to HYDRATECH data and a relationship from *Bünz et al.* [2005] for the central Norwegian margin (labelled "Storegga"). Velocities for gas-bearing sediments can be distinguished clearly. (A) shows the presence of free gas in the layer just below the BSR at site $N_3$ but also in the layers at greater depth. (B) shows the presence of undercompacted sediments at about 180 m depth below the seafloor.

Figure 7: Gas hydrate and free gas saturation estimates for the disseminated models. For each site the concentration of hydrate and gas is given for the three different approaches; P- and S-wave background velocities are represented by the back curves; the P- and S-wave seismic velocities extracted from our modelling are represented by dashed lines; the porosity and clay content used to define the background velocities are also shown and superimposed on the porosity log from ODP 986 (see Figure 1 for location).

Figure 8: Hydrate and free gas saturation estimates for the fracture models. The background velocities used are shown in Figure 6.

Figure 9: Schematic representation of the gas hydrate system along the Svalbard margin showing the variation in the hydrate formation and saturation depending on the type of sediment. a) Near the shelf break the sediments are dominated by coarse glacio-marine material with high velocity and low porosity, as seen on site $S_2$. Here the hydrate forms in relatively small quantities (up to 5%) as inclusions in the sediment; b) Further down the shelf, in the basin, hemipelagic sediments are present (site $N_3$) and hydrate is interpreted to form as part of the load-bearing framework above the base of the GSHZ with concentration twice as large as in the glacio-marine sequence.

Table captions:

Table 1: RMS and $\chi^2$ of final P-wave and S-wave velocity model at each site. The values given are for the models oriented W-E in the north, and SW-NE in the south. The total number of picks is also indicated for each model.

Table 2: Background velocities and assumed porosity and clay content are given for the three sites below the upper limit of the GHSZ.

*Acknowledgements: We thank the officers, crew and science party of the James Clark Ross cruise 211 for their assistance at sea. This work was supported by the UK National Environment Research Council (NERC) International Polar Year Programme (grant NE/D005723). The ocean-bottom instruments and associated sea-going technical support were provided by the Ocean-Bottom Instrumentation Facility, part of the NERC's Geophysical Equipment Facility.*

REFERENCES

Andreassen, K., et al. (1995), Seismic studies of a bottom simulating reflection related to gas hydrate beneath the continental margin of the Beaufort Sea, *J. Geophys. Res.*, *100*(B7), 12659-12673.

Archer, D., and B. Buffett (2005), Time-dependent response of the global ocean clathrate reservoir to climatic and anthropogenic forcing, *Geochem. Geophys. Geosyst.*, *6*(3), Q03002.

Bünz, S., and J. Mienert (2004), Acoustic imaging of gas hydrate and free gas at the Storegga Slide, *J. Geophys. Res.*, *109*(B4), B04102.

Bünz, S., et al. (2005), Gas hydrates at the Storegga Slide: Constraints from an analysis of multicomponent, wide-angle seismic data, *Geophysics*, *70*(5), B19-B34.

Chand, S., et al. (2004), Elastic velocity models for gas-hydrate-bearing sediments—a comparison, *Geophysical Journal International*, *159*(2), 573-590.

Chand, S., et al. (2006), An effective medium inversion algorithm for gas hydrate quantification and its application to laboratory and borehole measurements of gas hydrate-bearing sediments, *Geophysical Journal International*, *166*(2), 543-552.

Dickens, G. R. (1999), Carbon cycle: The blast in the past, *Nature*, *401*(6755), 752-755.

Dickson, B. (1999), Oceanography: All change in the Arctic, *Nature*, *397*(6718), 389-391.

Ecker, C., et al. (1998), Sediments with gas hydrates: Internal structure from seismic AVO, *Geophysics*, *63*(5), 1659-1669.

Eiken, O., and K. Hinz (1993), Contourites in the Fram Strait, *Sedimentary Geology*, *82*(1-4), 15-32.

Faleide, J. I., et al. (1993), Late Mesozoic-Cenozoic evolution of the south-western Barents Sea in a regional rift-shear tectonic setting, *Marine and Petroleum Geology*, *10*(3), 186-214.

Hamilton, E. L. (1980), Geoacoustic modeling of the sea floor, *The Journal of the Acoustical Society of America*, *68*(5), 1313-1340.

Harland, W. B., et al. (1997), Chapter 9 Central western Spitsbergen, *Geological Society, London, Memoirs*, *17*(1), 154-178.

Helgerud, M. B., et al. (1999), Elastic wave velocity in marine sediments with gas hydrates: Effective medium modeling, *Geophys. Res. Lett.*, *26*(13), 2021-2024.

Helgerud, M. B., et al. (2009), Elastic wave speeds and moduli in polycrystalline ice Ih, sI methane hydrate, and sII methane-ethane hydrate, *J. Geophys. Res.*, *114*(B2), B02212.

Holbrook, W. S., et al. (1996), Methane Hydrate and Free Gas on the Blake Ridge from Vertical Seismic Profiling, *Science*, *273*(5283), 1840-1843.

Hustoft, S., et al. (2009), Gas hydrate reservoir and active methane-venting province in sediments on < 20 Ma young oceanic crust in the Fram Strait, offshore NW-Svalbard, *Earth and Planetary Science Letters*, *284*(1-2), 12-24.

Jakobsen, M., et al. (2000), Elastic properties of hydrate-bearing sediments using effective medium theory, *J. Geophys. Res.*, *105*(B1), 561-577.

Johannessen, O. M., et al. (2004), Arctic climate change: observed and modeled temperature and sea-ice variability, *Tellus A*, *56*(5), 559-560.

Kennett, J. P., et al. (2000), Carbon Isotopic Evidence for Methane Hydrate Instability During Quaternary Interstadials, *Science*, *288*(5463), 128-133.

Kvenvolden, K. A. (1993), Gas hydrates;geological perspective and global change, *Rev. Geophys.*, *31*(2), 173-187.

Kvenvolden, K. A. (1999), Potential effects of gas hydrate on human welfare, *Proc. Natl. Acad. Sci. U. S. A.*, *96*(7), 3420-3426.

Liu, X., and P. B. Flemings (2007), Dynamic multiphase flow model of hydrate formation in marine sediments, *J. Geophys. Res.*, *112*(B3), B03101.

McGinnis, D. F., et al. (2006), Fate of rising methane bubbles in stratified waters: How much methane reaches the atmosphere?, *J. Geophys. Res.*, *111*(C9), C09007.

Mienert, J., et al. (1998), Gas hydrates along the northeastern Atlantic margin: possible hydrate-bound margin instabilities and possible release of methane, *Geological Society, London, Special Publications*, *137*(1), 275-291.

Mienert, J., et al. (2005), Ocean warming and gas hydrate stability on the mid-Norwegian margin at the Storegga Slide, *Marine and Petroleum Geology*, *22*(1-2), 233-244.

Minshull, T. A., and S. Chand (2009), The pore-scale distribution of sediment-hosted hydrates: evidence from effective medium modelling of laboratory and borehole seismic data, *Geological Society, London, Special Publications*, *319*(1), 93-101.

Minshull T. A, et al., (2005), Multi-disciplinary, sub-seabed geophysical imaging, *Sea Technology,* 46(10), 37-31.

Moridis, G. J. (2003), Numerical Studies of Gas Production From Methane Hydrates, *SPE Journal*, *32*(8), 359-370.

Myhre, A. M., et al. (Eds.) (1995), *Shipboard Scientific Party, Site 911*, 271-318 pp., College Station, TX.

Nisbet, E. G. (2002), Have sudden large releases of methane from geological reservoirs occurred since the Last Glacial Maximum, and could such releases occur again?, *Philosophical Transactions of the Royal Society of London. Series A: Mathematical, Physical and Engineering Sciences*, *360*(1793), 581-607.

Plaza-Faverola, A., et al. (2010), Evidence from three-dimensional seismic tomography for a substantial accumulation of gas hydrate in a fluid-escape chimney in the Nyegga pockmark field, offshore Norway, *J. Geophys. Res.*, *115*(B8), B08104.

Press, W., et al. (1992), *Numerical Recipes in Fortran 77: The Art of Scientific Computing*, Cambridge University Press.

Reagan, M. T., and G. J. Moridis (2008), Dynamic response of oceanic hydrate deposits to ocean temperature change, *J. Geophys. Res.*, *113*(C12), C12023.

Sarkar, S., et al. (in review), Switching of a paleo-ice stream in northwest Svalbard, *Quaternary Science Reviews*.

Schultheiss, P., et al. (2009), Wireline coring and analysis under pressure: Recent use and future developments of the HYACINTH system, *Scientific Drilling*, *7*, 44-50.

Singh, S. C., et al. (1993), Velocity Structure of a Gas Hydrate Reflector, *Science*, *260*(5105), 204-207.

Sowers, T. (2006), Late Quaternary Atmospheric CH4 Isotope Record Suggests Marine Clathrates Are Stable, *Science*, *311*(5762), 838-840.

Tréhu, A. M., et al. (2004), Three-dimensional distribution of gas hydrate beneath southern Hydrate Ridge: constraints from ODP Leg 204, *Earth and Planetary Science Letters*, *222*(3-4), 845-862.

Vogt, P. R., et al. (1994), Methane-generated(?) pockmarks on young, thickly sedimented oceanic crust in the Arctic: Vestnesa ridge, Fram strait, *Geology*, *22*(3), 255-258.

Vorren, T. O., and J. S. Laberg (1997), Trough mouth fans -- palaeoclimate and ice-sheet monitors, *Quaternary Science Reviews*, *16*(8), 865-881.

Vorren, T. O., et al. (1998), The Norwegian-Greenland Sea continental margins: morphology and late quaternary sedimentary processes and environment, *Quaternary Science Reviews*, *17*(1-3), 273-302.

Westbrook, G. K., et al. (2008), Estimation of gas hydrate concentration from multi-component seismic data at sites on the continental margins of NW Svalbard and the Storegga region of Norway, *Marine and Petroleum Geology*, *25*(8), 744-758.

Westbrook, G. K., et al. (2009), Escape of methane gas from the seabed along the West Spitsbergen continental margin, *Geophys. Res. Lett.*, *36*(15), L15608.

Zelt, C. A., and R. B. Smith (1992), Seismic traveltime inversion for 2-D crustal velocity structure, *Geophysical Journal International*, *108*(1), 16-34.

Zelt, C. A. (1999), Modelling strategies and model assessment for wide-angle seismic traveltime data, *Geophysical Journal International*, *139*(1), 183-204.

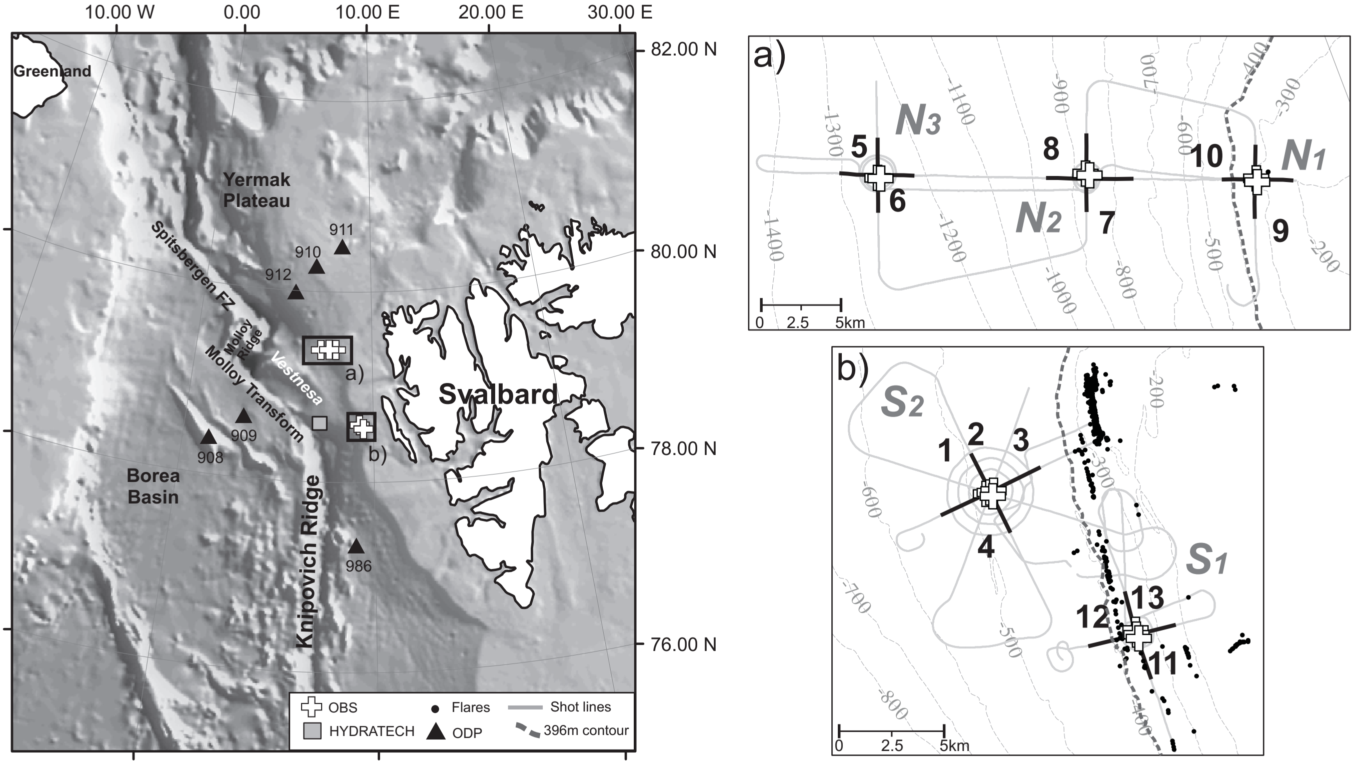

10.00 W
0.00
10.00 E
20.00 E
30.00 E
82.00 N
80.00 N
78.00 N
76.00 N
Greenland
Yermak Plateau
Spitsbergen FZ
Molloy Ridge
Molloy Transform
Vestnesa
Svalbard
Borea Basin
Knipovich Ridge
911
910
912
909
908
986
a)
b)
OBS
HYDRATECH
Flares
ODP
Shot lines
396m contour
N3
N2
N1
S2
S1
0
2.5
5km

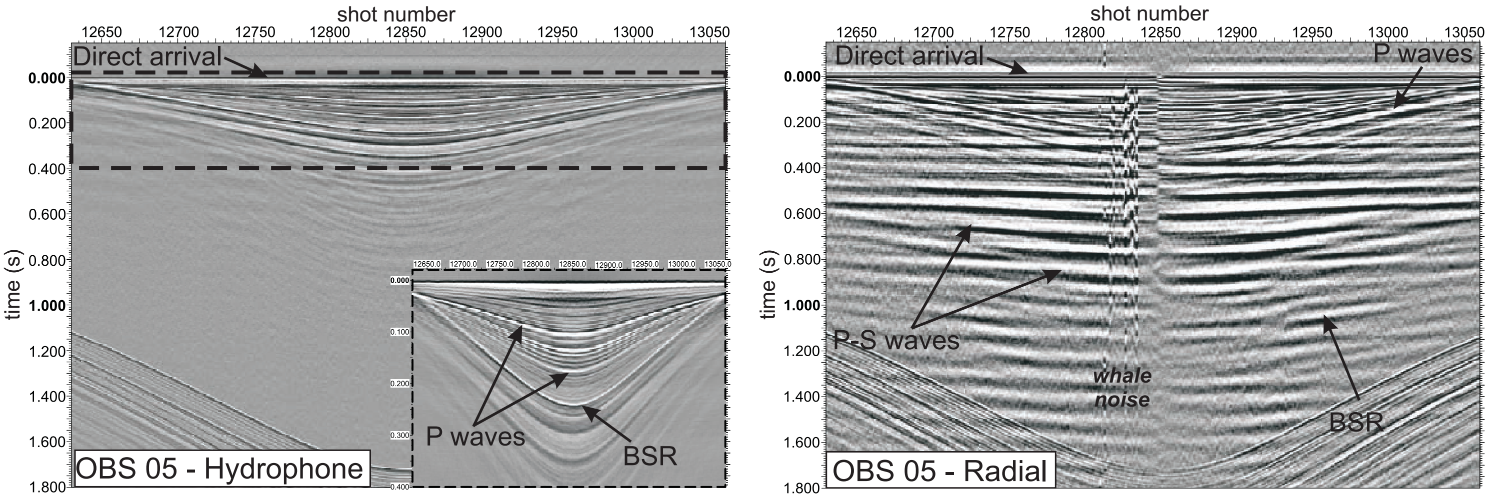
shot number
Direct arrival
time (s)
P waves
BSR
OBS 05 - Hydrophone
shot number
Direct arrival
P waves
P-S waves
whale noise
BSR
OBS 05 - Radial

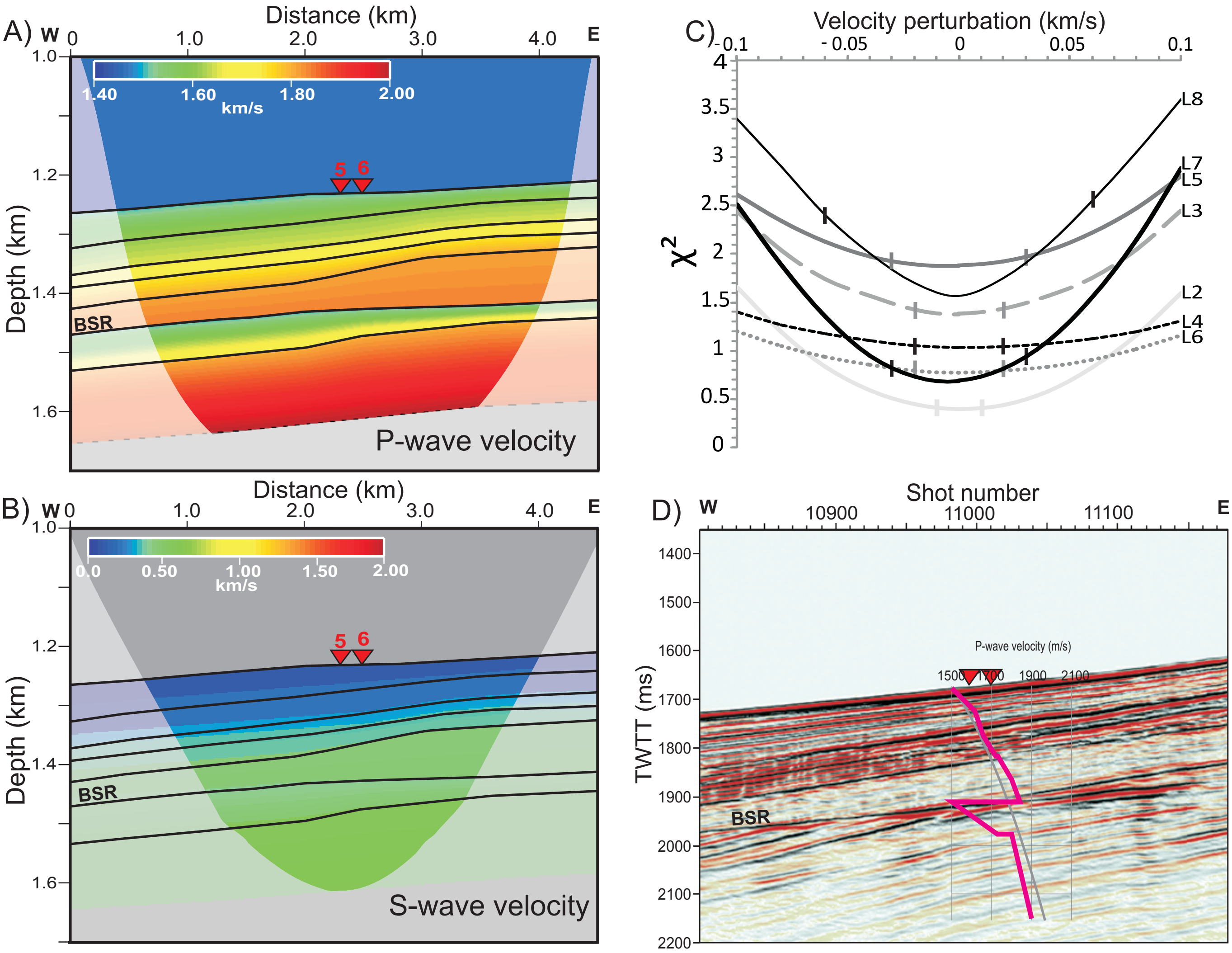
A)
Distance (km)
W
E
0
1.0
2.0
3.0
4.0
1.40
1.60
1.80
2.00
km/s
5
6
Depth (km)
1.0
1.2
1.4
1.6
BSR
P-wave velocity
B)
Distance (km)
S-wave velocity
0.0
0.50
1.00
1.50
2.00
C)
Velocity perturbation (km/s)
-0.1
- 0.05
0
0.05
0.1
$\chi^2$
4
3.5
3
2.5
2
1.5
1
0.5
0
L8
L7
L5
L3
L2
L4
L6
D)
Shot number
10900
11000
11100
TWTT (ms)
1400
1500
1600
1700
1800
1900
2000
2100
2200
P-wave velocity (m/s)
1500
1700
1900
2100
BSR

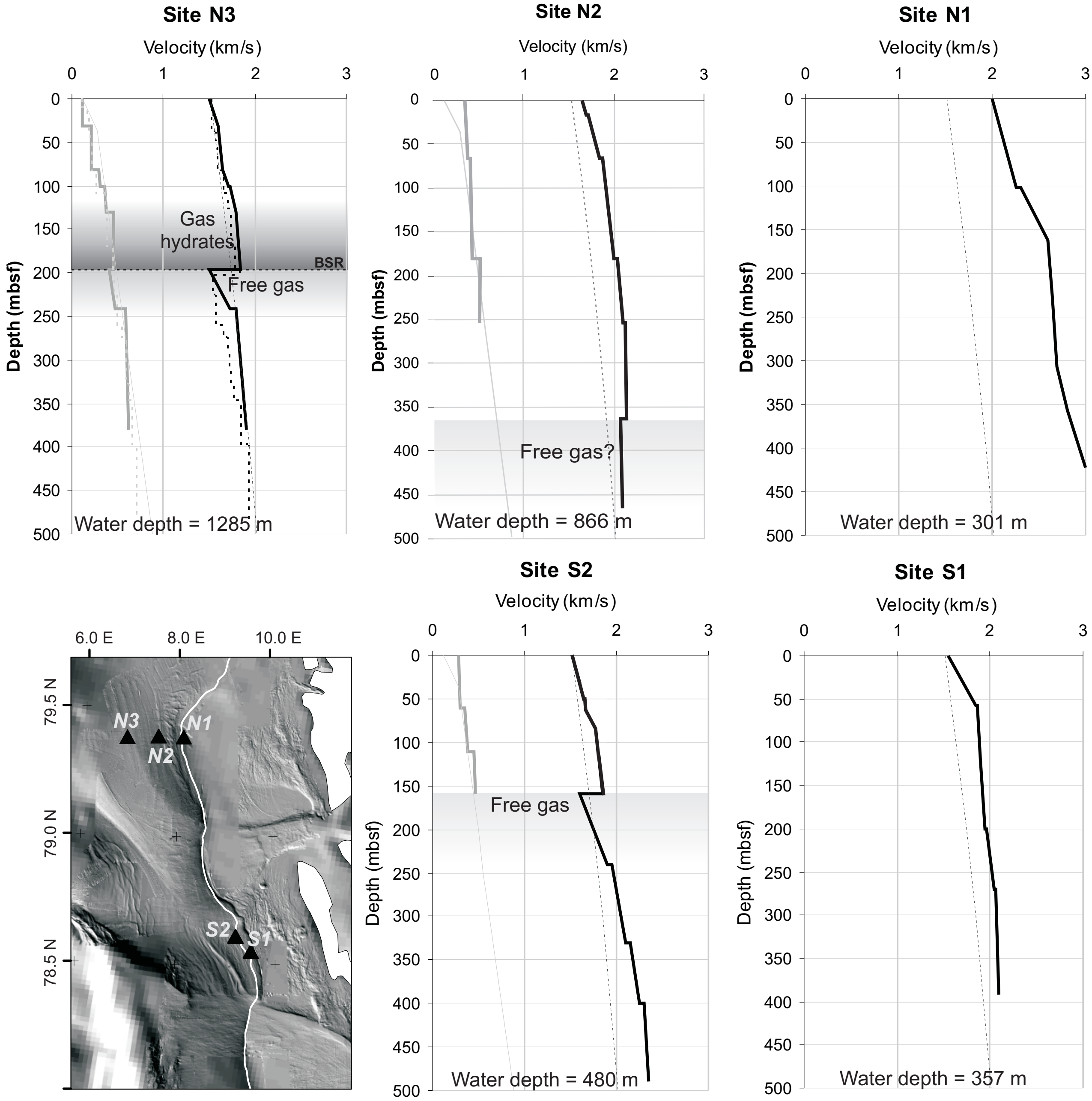

Site N3
Velocity (km/s)
Depth (mbsf)
Gas hydrates
BSR
Free gas
Water depth = 1285 m
Site N2
Velocity (km/s)
Depth (mbsf)
Free gas?
Water depth = 866 m
Site N1
Velocity (km/s)
Depth (mbsf)
Water depth = 301 m
6.0 E
8.0 E
10.0 E
79.5 N
79.0 N
78.5 N
N3
N2
N1
S2
S1
Site S2
Velocity (km/s)
Depth (mbsf)
Free gas
Water depth = 480 m
Site S1
Velocity (km/s)
Depth (mbsf)
Water depth = 357 m

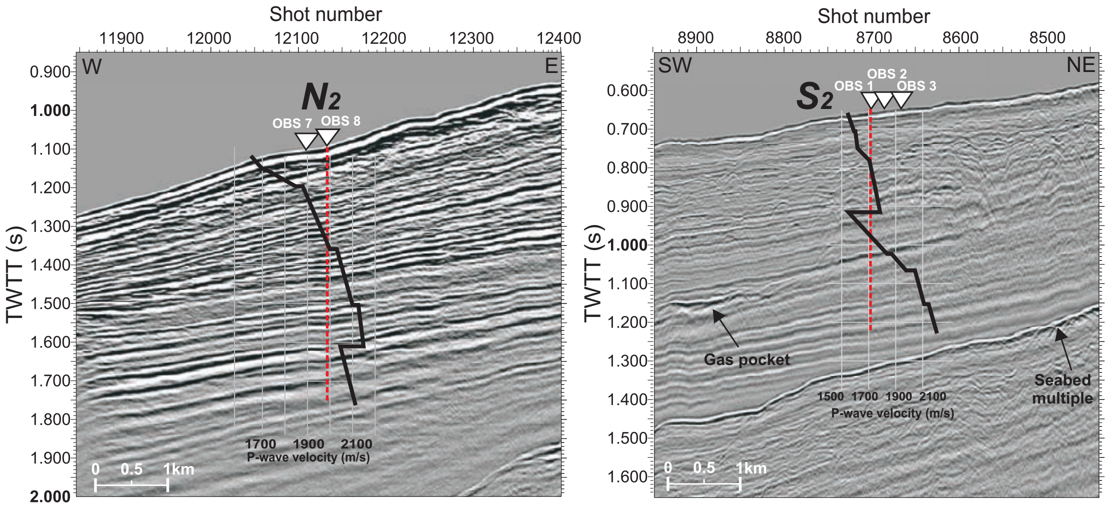

Shot number
11900 12000 12100 12200 12300 12400
W
E
N2
OBS 7
OBS 8
TWTT (s)
0.900
1.000
1.100
1.200
1.300
1.400
1.500
1.600
1.700
1.800
1.900
2.000
1700 1900 2100
P-wave velocity (m/s)
0 0.5 1km
Shot number
8900 8800 8700 8600 8500
SW
NE
S2
OBS 1
OBS 2
OBS 3
0.600
0.700
0.800
0.900
1.000
1.100
1.200
1.300
1.400
1.500
1.600
Gas pocket
1500 1700 1900 2100
P-wave velocity (m/s)
Seabed multiple
0 0.5 1km

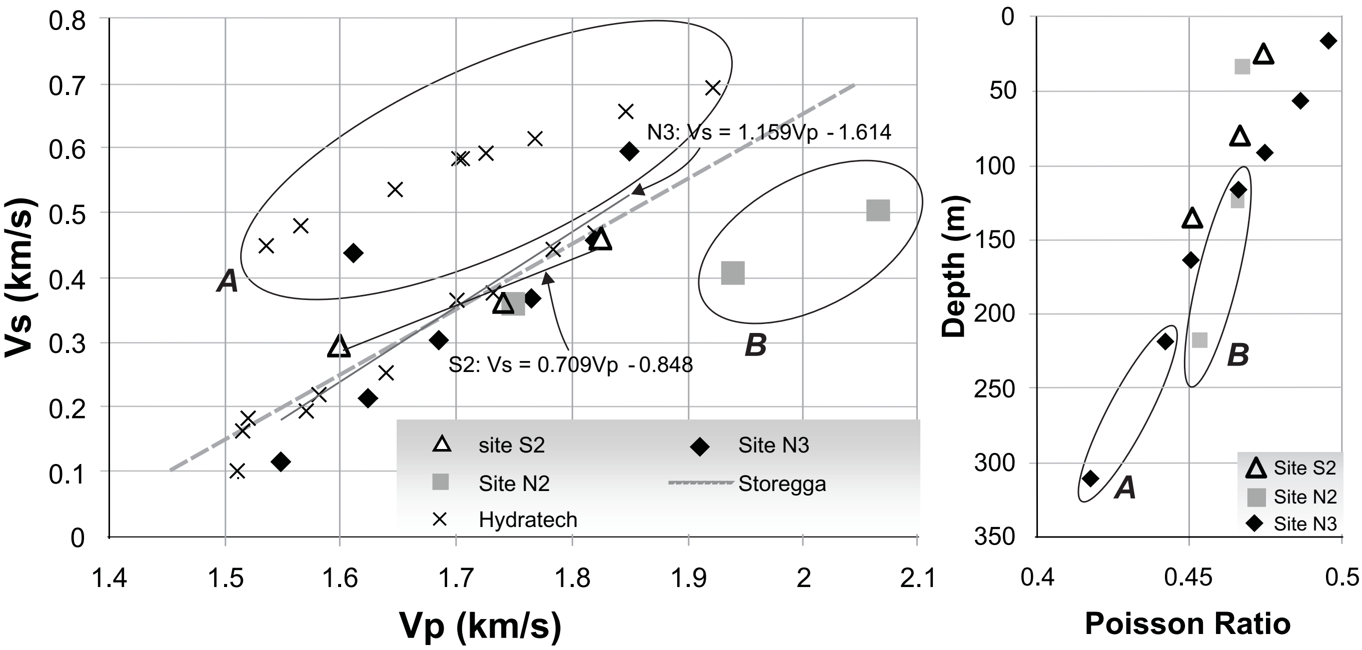

Vs (km/s)
Vp (km/s)
N3: Vs = 1.159Vp - 1.614
S2: Vs = 0.709Vp - 0.848
A
B
site S2
Site N2
Hydratech
Site N3
Storegga
Depth (m)
Poisson Ratio
Site S2
Site N2
Site N3

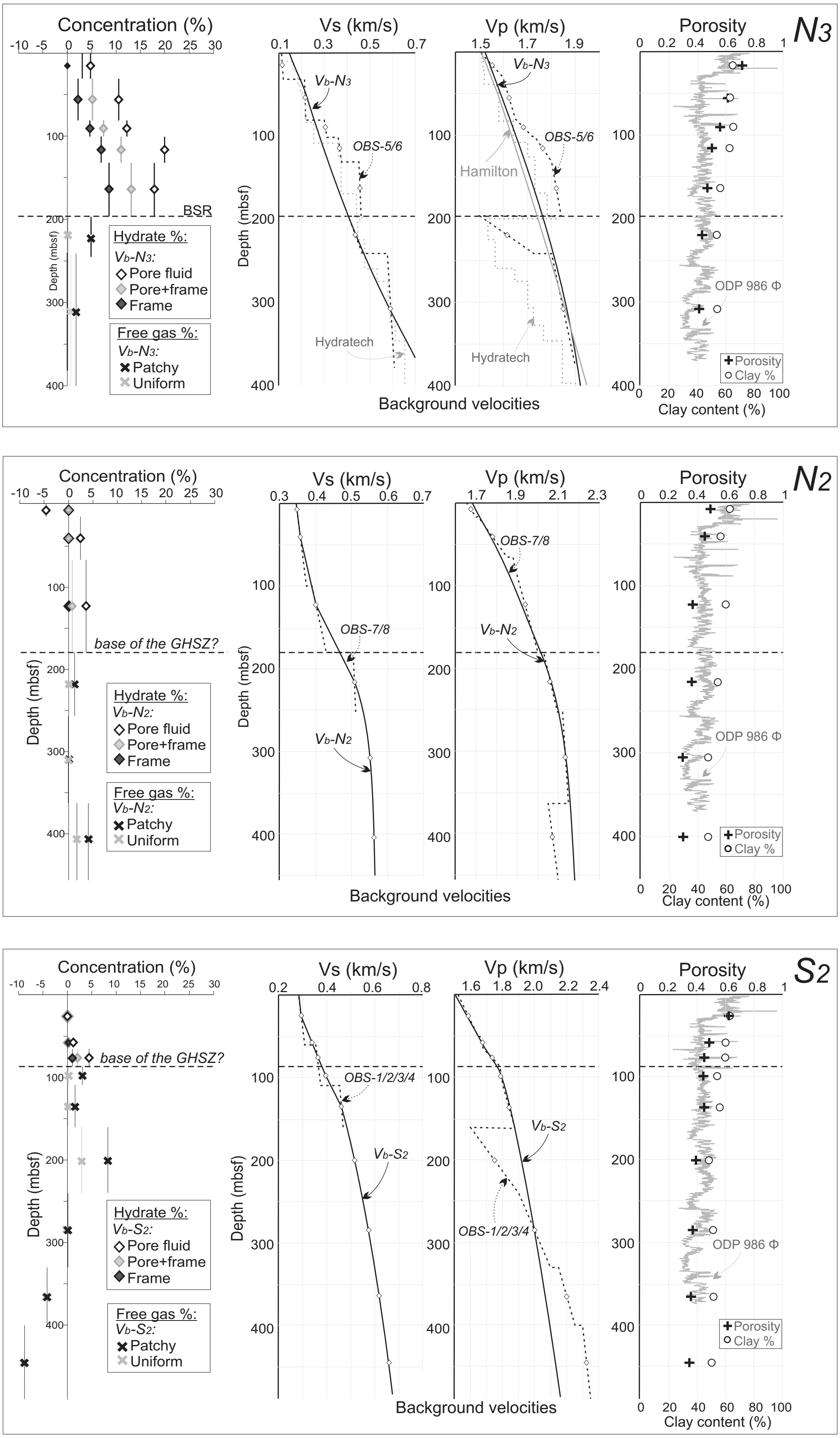
N3
Concentration (%)
-10 -5 0 5 10 15 20 25 30
BSR
Depth (mbsf)
Hydrate %:
Vb-N3:
Pore fluid
Pore+frame
Frame
Free gas %:
Vb-N3:
Patchy
Uniform
Vs (km/s)
0.1 0.3 0.5 0.7
Vb-N3
OBS-5/6
Hydratech
Vp (km/s)
1.5 1.7 1.9
Vb-N3
OBS-5/6
Hamilton
Hydratech
Background velocities
Porosity
0 0.2 0.4 0.6 0.8 1
ODP 986 Φ
Porosity
Clay %
0 20 40 60 80 100
Clay content (%)
N2
Concentration (%)
-10 -5 0 5 10 15 20 25 30
base of the GHSZ?
Depth (mbsf)
Hydrate %:
Vb-N2:
Pore fluid
Pore+frame
Frame
Free gas %:
Vb-N2:
Patchy
Uniform
Vs (km/s)
0.3 0.4 0.5 0.6 0.7
OBS-7/8
Vb-N2
Vp (km/s)
1.7 1.9 2.1 2.3
OBS-7/8
Vb-N2
Background velocities
Porosity
0 0.2 0.4 0.6 0.8 1
ODP 986 Φ
Porosity
Clay %
0 20 40 60 80 100
Clay content (%)
S2
Concentration (%)
-10 -5 0 5 10 15 20 25 30
base of the GHSZ?
Depth (mbsf)
Hydrate %:
Vb-S2:
Pore fluid
Pore+frame
Frame
Free gas %:
Vb-S2:
Patchy
Uniform
Vs (km/s)
0.2 0.4 0.6 0.8
OBS-1/2/3/4
Vb-S2
Vp (km/s)
1.6 1.8 2.0 2.2 2.4
Vb-S2
OBS-1/2/3/4
Background velocities
Porosity
0 0.2 0.4 0.6 0.8 1
ODP 986 Φ
Porosity
Clay %
0 20 40 60 80 100
Clay content (%)

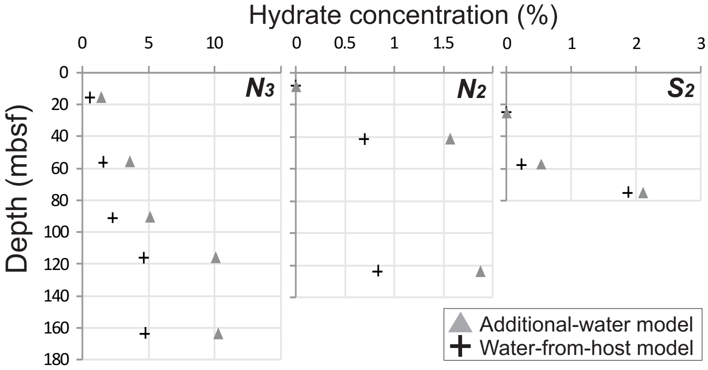
Hydrate concentration (%)
Depth (mbsf)
N3
N2
S2
Additional-water model
Water-from-host model

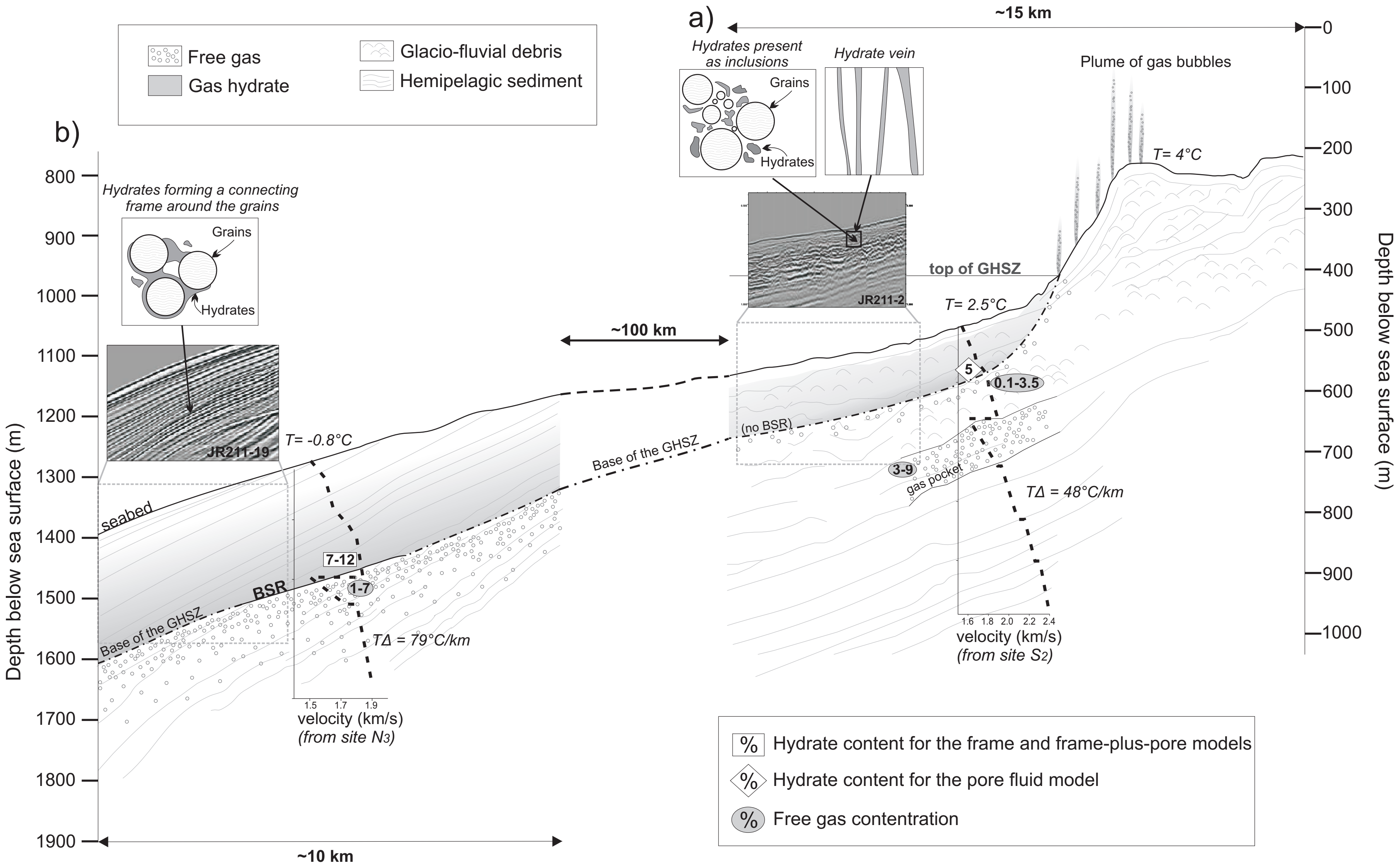

Free gas
Gas hydrate
Glacio-fluvial debris
Hemipelagic sediment
a)
~15 km
Hydrates present as inclusions
Grains
Hydrates
Hydrate vein
Plume of gas bubbles
T= 4°C
top of GHSZ
JR211-2
T= 2.5°C
5
0.1-3.5
(no BSR)
Base of the GHSZ
3-9
gas pocket
TΔ = 48°C/km
velocity (km/s)
(from site S2)
Depth below sea surface (m)
b)
Hydrates forming a connecting frame around the grains
Grains
Hydrates
JR211-19
T= -0.8°C
~100 km
seabed
7-12
BSR
1-7
Base of the GHSZ
TΔ = 79°C/km
velocity (km/s)
(from site N3)
Depth below sea surface (m)
~10 km
Hydrate content for the frame and frame-plus-pore models
Hydrate content for the pore fluid model
Free gas contentration

| **P-waves** | | | | | |
|---|---|---|---|---|---|
| | $N_3$ | $N_2$ | $N_1$ | $S_2$ | $S_1$ |
| **Nb of picks** | 6582 | 3374 | 1324 | 4866 | 1983 |
| **RMS** | 0.004 | 0.004 | 0.007 | 0.005 | 0.006 |
| **$\chi^2$** | 0.899 | 1.002 | 1.540 | 1.182 | 1.455 |

| **S-waves** | | | | | |
|---|---|---|---|---|---|
| | $N_3$ | $N_2$ | $N_1$ | $S_2$ | $S_1$ |
| **Nb of picks** | 1770 | 776 | - | 309 | - |
| **RMS** | 0.006 | 0.005 | - | 0.005 | - |
| **$\chi^2$** | 1.349 | 1.005 | - | 1.583 | - |

| Depth | Vp | Vp backgrd | Vs | Vs backgrd | Vp/Vs | Poisson Ratio | Porosity | Clay % |
|---|---|---|---|---|---|---|---|---|
| **N3** | | | | | | | | |
| 15.5 | 1.55 | 1.542 | 0.115 | 0.175 | 13.4783 | 0.4959 | 0.73 | 66 |
| 56 | 1.625 | 1.595 | 0.216 | 0.22 | 7.5231 | 0.4866 | 0.61 | 62 |
| 91 | 1.685 | 1.638 | 0.305 | 0.264 | 5.5246 | 0.4750 | 0.55 | 66 |
| 116 | 1.765 | 1.673 | 0.37 | 0.298 | 4.7703 | 0.4663 | 0.5 | 61 |
| 163.5 | 1.82 | 1.72 | 0.459 | 0.371 | 3.9651 | 0.4507 | 0.48 | 58 |
| 219 | 1.6125 | 1.785 | 0.438 | 0.438 | 3.6815 | 0.4425 | 0.43 | 54 |
| 311.5 | 1.85 | 1.865 | 0.596 | 0.596 | 3.1040 | 0.4179 | 0.41 | 55 |
| **N2** | | | | | | | | |
| 8.625 | 1.675 | 1.7 | 0.348 | 0.348 | 4.8132 | 0.4669 | 0.48 | 61 |
| 41.625 | 1.78 | 1.772 | 0.358 | 0.358 | 4.9721 | 0.4690 | 0.42 | 56 |
| 123.5 | 1.94 | 1.93 | 0.401 | 0.401 | 4.8379 | 0.4673 | 0.37 | 60 |
| 217.25 | 2.075 | 2.075 | 0.508 | 0.508 | 4.0846 | 0.4537 | 0.36 | 55 |
| 308.5 | 2.135 | 2.135 | 0.507 | 0.507 | 4.2110 | 0.4565 | 0.31 | 49 |
| 413.5 | 2.075 | 2183 | 0.53 | 0.53 | 3.9151 | 0.4494 | 0.29 | 43 |
| **S2** | | | | | | | | |
| 25 | 1.525 | 1.52 | 0.295 | 0.295 | 5.1695 | 0.4714 | 0.63 | 64 |
| 57.5 | 1.675 | 1.675 | 0.337 | 0.337 | 4.9703 | 0.4690 | 0.48 | 60 |
| 75 | 1.73 | 1.72 | 0.362 | 0.362 | 4.7790 | 0.4664 | 0.45 | 60 |
| 97.5 | 1.79 | 1.8 | 0.395 | 0.395 | 4.5316 | 0.4626 | 0.44 | 55 |
| 135 | 1.825 | 1.82 | 0.461 | 0.461 | 3.9588 | 0.4506 | 0.45 | 57 |
| 200 | 1.75 | 1.916 | 0.508 | 0.508 | 3.4449 | 0.4340 | 0.39 | 49 |
| 285 | 2 | 2 | 0.589 | 0.589 | 3.3956 | 0.4320 | 0.38 | 53 |
| 365 | 2.2 | 2.07 | 0.67 | 0.67 | 3.2836 | 0.4271 | 0.37 | 56 |
| 445 | 2.325 | 2.135 | 0.748 | 0.748 | 3.1083 | 0.4181 | 0.36 | 43 |